Article

Vapor–Liquid–Solid and Vapor–Solid Growth of Phase-Change Sb_2Te_3 Nanowires and Sb_2Te_3/GeTe Nanowire Heterostructures

Jin Seok Lee, Sarah Brittman, Dong Yu, and Hongkun Park

J. Am. Chem. Soc., **2008**, 130 (19), 6252-6258 • DOI: 10.1021/ja711481b • Publication Date (Web): 11 April 2008

J|A|C|S
ARTICLES

Published on Web 04/11/2008

Vapor–Liquid–Solid and Vapor–Solid Growth of Phase-Change Sb_2Te_3 Nanowires and Sb_2Te_3/GeTe Nanowire Heterostructures

Jin Seok Lee, Sarah Brittman, Dong Yu, and Hongkun Park*

Department of Chemistry and Chemical Biology, Harvard University, 12 Oxford Street, Cambridge, Massachusetts 02138

Received December 30, 2007; E-mail: Hongkun_Park@harvard.edu

Abstract: We report the synthesis and characterization of radial heterostructures composed of an antimony telluride (Sb_2Te_3) core and a germanium telluride (GeTe) shell, as well as an improved synthesis of Sb_2Te_3 nanowires. The synthesis of the heterostructures employs Au-catalyst-assisted vapor–liquid–solid (VLS) and vapor−solid (VS) mechanisms. Energy-dispersive X-ray spectrometry indicates that Sb and Ge are localized in the Sb_2Te_3 and GeTe portions, respectively, confirming the alloy-free composition in the core/shell heterostructures. Transmission electron microscopy and diffraction studies show that Sb_2Te_3 and GeTe regions exhibit rhombohedral crystal structure. Both Sb_2Te_3 and GeTe grow along the [110] direction with an epitaxial interface between them. Electrical characterization of individual nanowires and nanowire heterostructures demonstrates that these nanostructures exhibit memory-switching behavior.

Introduction

Chalcogenides exhibit a reversible crystalline−amorphous phase change induced by temperature or electric field and have been the subject of numerous research activities.[1–5] Because the phase change is accompanied by dramatic differences in optical reflectivity[2] and electrical resistivity,[1] these materials can be the basis of data storage media such as CD/DVD[3] and phase-change random access memory (PRAM).[5] In principle, PRAM exhibits many potential advantages over conventional electronic memory, including fast access time, low power consumption, low cost, scalability, and nonvolatility;[6] consequently, the electronics industry has been actively developing and testing PRAM for future nonvolatile memory applications.

The intrinsic properties of chalcogenide materials and their size-dependent variations determine the speed, stability, and miniaturization of PRAM. The most commonly researched chalcogenide glasses contain a combination of Ge, Sb, and Te, sometimes with various dopants.[4] Considerable work has focused on germanium antimony telluride (GST), in particular with a composition $Ge_2Sb_2Te_5$, as a promising compromise between the stable, slowly switching germanium telluride (GeTe) and the less stable, rapidly switching antimony telluride (Sb_2Te_3).[7,8] The exact mechanism of the phase change in chalcogenide glasses, however, is still under debate,[9–11] and the evolution of the phase-change properties as the structure's dimensions reach the nanoscale is just beginning to be investigated.[12–14] Investigating at the nanoscale the extremes of this family, such as Sb_2Te_3 and GeTe, will offer a fuller sense of the chemistry and physics behind these materials.

Over the past decades, one-dimensional nanostructures[15,16] of various materials[17–24] and of different morphologies[25–37] have

(1) Ovshinsky, S. R. *Phys. Rev. Lett.* **1968**, *21*, 1450–1453.
(2) Feinleib, J.; Deneufville, J.; Moss, S. C.; Ovshinsky, S. R. *Appl. Phys. Lett.* **1971**, *18*, 254–257.
(3) Yamada, N.; Ohno, E.; Nishiuchi, K.; Akahira, N.; Takao, M. *J. Appl. Phys.* **1991**, *69*, 2849–2856.
(4) Hudgens, S.; Johnson, B. *MRS Bull.* **2004**, *29*, 829–832.
(5) Lankhorst, M. H. R.; Ketelaars, B.; Wolters, R. A. M. *Nat. Mater.* **2005**, *4*, 347–352.
(6) Lai, S. *IEDM Tech. Dig.* **2003**, 255–258.
(7) Chen, Y. C.; Chen, C. T.; Yu, J. Y.; Lee, C. Y.; Chen, C. F.; Lung, S. L.; Liu, R. *Proc. IEEE Cus. Int. Cir. Conf.* **2003**, 395–398.
(8) Strand, D. *J. Optoelectron. Adv. Mater.* **2005**, *7*, 1679–1690.
(9) Adler, D.; Henisch, H. K.; Mott, N. *Rev. Mod. Phys.* **1978**, *50*, 209–220.
(10) Adler, D.; Shur, M. S.; Silver, M.; Ovshinsky, S. R. *J. Appl. Phys.* **1980**, *51*, 3289–3309.
(11) Greer, A. L.; Mathur, N. *Nature* **2005**, *437*, 1246–1247.
(12) Yu, D.; Wu, J.; Gu, Q.; Park, H. *J. Am. Chem. Soc.* **2006**, *128*, 8148–8149.
(13) Lee, S.-H.; Ko, D.-K.; Jung, Y.; Agarwal, R. *Appl. Phys. Lett.* **2006**, *89*, 223116.
(14) Lee, S.-H.; Jung, Y.; Agarwal, R. *Nat. Nanotechnol.* **2007**, *2*, 626–630.
(15) Xia, Y. N.; Yang, P. D.; Sun, Y. G.; Wu, Y. Y.; Mayers, B.; Gates, B.; Yin, Y. D.; Kim, F.; Yan, Y. Q. *Adv. Mater.* **2003**, *15*, 353–389.
(16) Law, M.; Goldberger, J.; Yang, P. D. *Annu. Rev. Mater. Res.* **2004**, *34*, 83–122.
(17) Huang, M. H.; Wu, Y. Y.; Feick, H.; Tran, N.; Weber, E.; Yang, P. D. *Adv. Mater.* **2001**, *13*, 113–116.
(18) Barrelet, C. J.; Wu, Y.; Bell, D. C.; Lieber, C. M. *J. Am. Chem. Soc.* **2003**, *125*, 11498–11499.
(19) Persson, A. I.; Larsson, M. W.; Stenstrom, S.; Ohlsson, B. J.; Samuelson, L.; Wallenberg, L. R. *Nat. Mater.* **2004**, *3*, 677–681.
(20) Zhang, D.; Liu, Z.; Han, S.; Li, C.; Lei, B.; Stewart, M. P.; Tour, J. M.; Zhou, C. *Nano Lett.* **2004**, *4*, 2151–2155.
(21) Cho, K. S.; Talapin, D. V.; Gaschler, W.; Murray, C. B. *J. Am. Chem. Soc.* **2005**, *127*, 7140–7147.
(22) Guiton, B. S.; Gu, Q.; Prieto, A. L.; Gudiksen, M. S.; Park, H. *J. Am. Chem. Soc.* **2005**, *127*, 498–499.
(23) Hor, Y. S.; Welp, U.; Ito, Y.; Xiao, Z. L.; Patel, U.; Mitchell, J. F.; Kwok, W. K.; Crabtree, G. W. *Appl. Phys. Lett.* **2005**, *87*, 142506.
(24) Gu, Q.; Falk, A.; Wu, J. Q.; Ouyang, L.; Park, H. *Nano Lett.* **2007**, *7*, 363–366.
(25) Hu, J. T.; Odom, T. W.; Lieber, C. M. *Acc. Chem. Res.* **1999**, *32*, 435–445.

10.1021/ja711481b CCC: $40.75

been successfully synthesized. Specifically for phase-change materials, GeTe,[12,13,38,39] Sb_2Te_3,[38] and $Ge_2Sb_2Te_5$[14,40] nanowires (NWs) have been synthesized by the vapor-transport method. Sb_2Te_3 nanostructures have also been synthesized by a variety of means, including the decomposition of a single-source precursor,[41] electrochemical deposition into porous alumina,[42] electrochemical atomic layer epitaxy,[43] and solvothermal,[44] colloidal,[45] solution-based,[46] and hydrothermal[47] processes. The memory-switching behavior of GeTe[12,13] and $Ge_2Sb_2Te_5$[14,40] NWs has been studied, but that of Sb_2Te_3 NWs has not been reported because NWs of sufficient length have not been synthesized.

Here, we report a metal-catalyzed vapor-transport method to synthesize Sb_2Te_3 and Sb_2Te_3/GeTe core/shell nanostructures with various morphologies. We then demonstrate the feasibility of their use for memory switching by investigating the electrical properties of individually contacted NWs. For the synthesis of the Sb_2Te_3 NWs, elemental precursors were located in different temperature regions of the furnace for compositional and morphological control.[40] The Sb_2Te_3 nanostructures exhibit a variety of controllable morphologies including thin/thick/zigzag-NWs, nanobelts, nanotubes, and microplates. The Sb_2Te_3/GeTe core/shell NW heterostructures were synthesized in two steps via an *in situ* exchange of precursors, followed by a change in reaction conditions. Transmission electron microscopy (TEM) and diffraction studies show that Sb_2Te_3 and GeTe regions of the nanostructures exhibit rhombohedral crystal structure. Both Sb_2Te_3 and GeTe grow along the [110] direction with an epitaxial interface between them. The growth mechanisms of the Sb_2Te_3 nanostructures and radial core/shell heterostructure have been studied in detail.

Experimental Section

Chemicals. GeTe (99.99%) and Te (−40 mesh, 99.997%) powders were purchased from Aldrich. Sb (−200 mesh, 99.999%) powder was purchased from Alfa Aesar. Poly-L-lysine (0.1% w/v aqueous solution) and colloidal Au nanoparticles (10 nm in diameter) were purchased from Ted Pella. Acetone and 2-propanol were purchased from VWR. Si/SiO_2 wafers were purchased from University Wafer.

Preparation of Au-Covered Substrates. Au nanoparticles, immobilized on the Si/SiO_2 substrate using a thin polyelectrolyte layer, acted as seeds for the growth of the nanostructures. Initially, the substrates were sonicated at 35 kHz for 2 min, first in 2-propanol and then in distilled deionized (DD) water, to remove organic residue and particles. The substrates were then treated in a piranha solution (H_2SO_4:30% H_2O_2 = 3:1) at 95–100 °C for 30 min to remove any remaining organic residue. The acid-treated substrates were washed with DD water and dried with high-purity nitrogen. A thin layer of polyelectrolyte was deposited on the substrates by immersing them in 0.1 wt % aqueous poly-L-lysine solution for 1 min. This polymer possesses a net positive charge in aqueous solution at neutral pH and adheres to the substrate through the electrostatic attraction to deprotonated hydroxyl groups on the silica. After being rinsed with DD water, the polyelectrolyte-coated substrates were immersed in the Au nanoparticle solution (10 nm in diameter). The positively charged polymer film attracts negatively charged Au nanoparticles. Following a final rinse with DD water and drying, the Au-covered substrates were used for nanostructure growth.

Synthesis of Sb_2Te_3 Nanostructures (NWs, NBs, and NTs). Sb_2Te_3 NWs were synthesized by the vapor-transport method in a 12 in. horizontal tube furnace (Lindberg/Blue M) equipped with a 1 in. diameter quartz tube. Elemental powders were used as precursors. The reaction setup is shown in Figure 1a. Based on the melting temperatures of Sb and Te (630 and 449 °C, respectively[48]) (Figure 1b), the temperature profile of the tube furnace and the spatial location of the precursors were adjusted to optimize the synthesis of Sb_2Te_3 nanostructures (Figure 1c). Sb powder was placed at the center of the heating zone, while Te powder was located 13.5 cm upstream from the Sb powder. A Si/SiO_2 substrate covered with Au nanoparticles was placed in the downstream zone of the furnace. Before the experiment, the quartz tube was evacuated to below 1 Torr and flushed repeatedly with Ar gas to minimize oxygen contamination. The furnace was then heated to the reaction temperature at 16.6 °C/min. The vapor-phase reactants transported by the Ar carrier gas condensed onto the substrate as various nanostructures depending on the reaction conditions. The optimal reaction temperature (T), pressure (P), time (t), and Ar flow rate (k_{flow}) for different nanostructure morphologies are listed in Figure 1d. The best location of the substrate for nanostructure growth was determined to be 9–11 cm downstream from the hot center of the furnace.

Synthesis of Sb_2Te_3/GeTe Core/Shell NW Heterostructures. For the synthesis of Sb_2Te_3/GeTe core/shell NWs, magnets were attached to each quartz transfer tube, allowing the *in situ* exchange of sources. Before the reaction, a few milligrams of Sb_2Te_3 and GeTe precursors were loaded into separate quartz transfer tubes. For growth of Sb_2Te_3 NWs, a quartz transfer tube containing Sb and Te powders separated by 13.5 cm was loaded, and the synthesis of the Sb_2Te_3 cores was performed using the procedure outlined above. After 3 h, growth of the Sb_2Te_3 cores was terminated by removing the tube containing the Sb and Te powders. The Si/SiO_2 substrate was then shifted 2 cm downstream to optimize the growth of GeTe shells (11–14 cm away from the hot center of the furnace).

(26) Pan, Z. W.; Dai, Z. R.; Wang, Z. L. *Science* **2001**, *291*, 1947–1949.
(27) Gudiksen, M. S.; Lauhon, L. J.; Wang, J.; Smith, D. C.; Lieber, C. M. *Nature* **2002**, *415*, 617–620.
(28) Lauhon, L. J.; Gudiksen, M. S.; Wang, C. L.; Lieber, C. M. *Nature* **2002**, *420*, 57–61.
(29) Wu, Y. Y.; Fan, R.; Yang, P. D. *Nano Lett.* **2002**, *2*, 83–86.
(30) Han, S.; Li, C.; Liu, Z.; Lei, B.; Zhang, D.; Jin, W.; Liu, X.; Tang, T.; Zhou, C. *Nano Lett.* **2004**, *4*, 1241–1246.
(31) Kong, X. Y.; Ding, Y.; Yang, R.; Wang, Z. L. *Science* **2004**, *303*, 1348–1351.
(32) Lauhon, L. J.; Gudiksen, M. S.; Lieber, C. M. *Philos. Trans. R. Soc. London A* **2004**, *362*, 1247–1260.
(33) Qian, F.; Li, Y.; Gradecak, S.; Wang, D. L.; Barrelet, C. J.; Lieber, C. M. *Nano Lett.* **2004**, *4*, 1975–1979.
(34) Yang, R. S.; Ding, Y.; Wang, Z. L. *Nano Lett.* **2004**, *4*, 1309–1312.
(35) Yang, C.; Zhong, Z. H.; Lieber, C. M. *Science* **2005**, *310*, 1304–1307.
(36) Jiang, X. C.; Xiong, Q. H.; Nam, S.; Qian, F.; Li, Y.; Lieber, C. M. *Nano Lett.* **2007**, *7*, 3214–3218.
(37) Kim, D.-W.; Hwang, I.-S.; Kwon, S. J.; Kang, H.-Y.; Park, K.-S.; Choi, Y.-J.; Choi, K.-J.; Park, J.-G. *Nano Lett.* **2007**, *7*, 3041–3045.
(38) Meister, S.; Peng, H.; McIlwrath, K.; Jarausch, K.; Zhang, X. F.; Cui, Y. *Nano Lett.* **2006**, *6*, 1514–1517.
(39) Sun, X.; Yu, B.; Ng, G.; Meyyappan, M. *J. Phys. Chem. C* **2007**, *111*, 2421–2425.
(40) Jung, Y.; Lee, S.-H.; Ko, D.-K.; Agarwal, R. *J. Am. Chem. Soc.* **2006**, *128*, 14026–14027.
(41) Garje, S. S.; Eisler, D. J.; Ritch, J. S.; Afzaal, M.; O'Brien, P.; Chivers, T. *J. Am. Chem. Soc.* **2006**, *128*, 3120–3121.
(42) Jin, C.; Zhang, G.; Qian, T.; Li, X.; Yao, Z. *J. Phys. Chem. B* **2005**, *109*, 1430–1432.
(43) Yang, J.; Zhu, W.; Gao, X.; Bao, S.; Fan, X.; Duan, X.; Hou, J. *J. Phys. Chem. B* **2006**, *110*, 4599–4604.
(44) Wang, W.; Poudel, B.; Yang, J.; Wang, D. Z.; Ren, Z. F. *J. Am. Chem. Soc.* **2005**, *127*, 13792–13793.
(45) Christian, P.; O'Brien, P. *J. Mater. Chem.* **2005**, *15*, 4949–4954.
(46) Karkamkar, A. J.; Kanatzidis, M. G. *J. Am. Chem. Soc.* **2006**, *128*, 6002–6003.
(47) Shi, W.; Yu, J.; Wang, H.; Zhang, H. *J. Am. Chem. Soc.* **2006**, *128*, 16490–16491.
(48) Okamoto, H.; Massaalski, T. B. *Phase Diagrams of Binary Gold Alloys*; ASM International: Metals Park, OH, 1987.

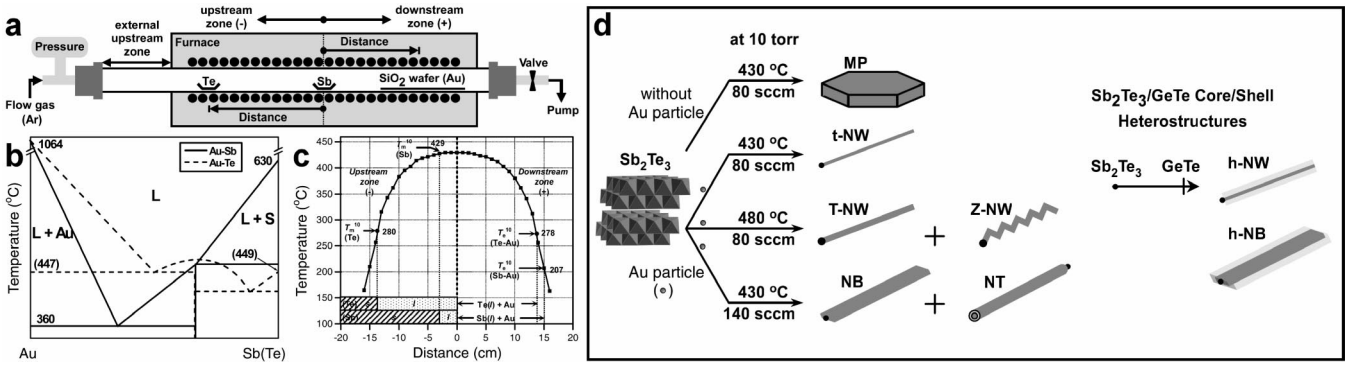

Figure 1. (a) Schematic of the furnace used for the synthesis of Sb_2Te_3 nanostructures. (b) Binary phase diagram between Au and Sb or Te: L, liquid; S, solid. (c) Temperature profile of the furnace at 430 °C: T_m^{10}, melting temperature at 10 Torr; T_e^{10}, eutectic temperature with Au at 10 Torr. (d) Morphologies of Sb_2Te_3 nanostructures controlled by the growth temperature and the Ar flow rate: MP, microplate; t-NW, thin NW; T-NW, thick NW; Z-NW, zigzag NW; NB, nanobelt; NT, nanotube; h-NW, core/shell NW heterostructure; h-NB, core/shell NB heterostructure.

The furnace's temperature was lowered to 400 °C and maintained without introducing GeTe precursors for 1 h to eliminate the Sb and Te precursors in the reaction tube. During this period, Ar was flowing at 140 sccm, and the total pressure was maintained at 10 Torr. Afterward, GeTe powder was inserted into the center of the heating zone to start deposition of the shell. The reaction time was 4 h, corresponding to the formation of a ~50 nm GeTe shell, according to TEM analysis.

Characterization of Products. The morphology of the Sb_2Te_3 NWs and Sb_2Te_3/GeTe core/shell NW heterostructures was analyzed with a LEO 982 field-emission scanning electron microscope (SEM) and a JEOL 2100/2010 transmission electron microscope (TEM) with scanning-mode TEM (STEM) imaging and energy-dispersive X-ray (EDX) mapping capabilities. The SEM imaging was performed on as-synthesized products at 10 kV. Samples for TEM imaging were made by depositing a solution of NWs (prepared by sonication of as-synthesized chips in hexane) onto holey, carbon 300 mesh copper grids (Structure Probe, Inc.) and were imaged at 200 kV. Powder X-ray diffraction (XRD) was performed at a scanning rate of 1 deg/min using a Scintag XDS2000 X-ray diffractometer with a Cu Kα radiation source ($\lambda = 1.5418$ Å).

Fabrication of Electrical Devices. After synthesis, the Sb_2Te_3 NWs or Sb_2Te_3/GeTe core/shell NW heterostructures were suspended in methanol by sonication, and 5 μL aliquots of these solutions were deposited repeatedly on a Si/SiO_2 substrate with a prepatterned grid. Electron-beam lithography was used to define electrical leads to individual nanostructures. To make low-resistance, ohmic contacts to the Sb_2Te_3 NWs, the chip was cleaned in an Ar plasma, and Cr (50 nm) and Au (150 nm) layers were deposited by sputtering, followed by liftoff. For contacts to the Sb_2Te_3/GeTe core/shell NW heterostructures, Ni (50 nm) and Au (150 nm) layers were thermally evaporated, followed by liftoff. Devices were imaged using SEM at 5 kV and then coated with a protective layer of silicon nitride using electron-beam evaporation. For the Sb_2Te_3 NWs, the distance between the electrodes along the wire ranged from 175 nm to 2 μm but was 600−900 nm for most devices. The diameters of NWs in devices measured ranged from 45 to 200 nm. For the Sb_2Te_3/GeTe core/shell NW heterostructures, the distance between the electrodes was 500 nm to 2 μm, and diameters ranged from 100 to 300 nm.

Electrical Measurements. In direct current (dc) voltage measurements, the voltage was increased at 100 mV/s, and a load resistor of 100 kΩ was used to limit the current after the phase transition; otherwise, the large current flowing through the crystalline phase destroyed the device. A pulse generator (Stanford Research System model DG535) produced the amorphization and recrystallization pulses, and the traces were monitored with a digital oscilloscope (Tektronix TDS2022).

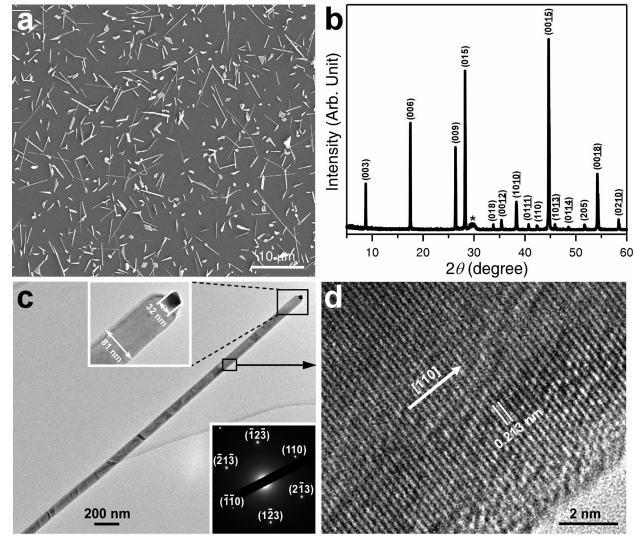

Figure 2. (a) SEM image and (b) XRD pattern of Sb_2Te_3 t-NWs. The XRD peak marked with an asterisk is from the Si/SiO_2 substrate. (c) TEM image of a Sb_2Te_3 t-NW. Insets of (c): top, high-magnification TEM image of the t-NW end with a Sb_xTe_y/Au alloy particle; bottom, SAED pattern indexed for rhombohedral Sb_2Te_3. (d) HRTEM image taken from the area designated in (c).

Results

In the synthesis of Sb_2Te_3 nanostructures, varying temperature and Ar flow rate allows considerable control over the morphology of the products (Figure 1d). Figure 2a and Figure S1b−d in the Supporting Information show representative SEM images of Sb_2Te_3 thin NWs (t-NWs), thick NWs (T-NWs) and zigzag NWs (Z-NWs), nanobelts (NBs), and microplates (MPs), respectively. These nanostructures were obtained from the growth conditions listed in Figure 1d. Analysis of SEM images of products from several reactions shows that the average diameter of t-NWs is 73 ± 21 nm, with lengths up to 20 μm, whereas the average diameter of the T-NWs/Z-NWs mixture is 157 ± 44 nm. The average width of the NBs is 257 ± 101 nm (Figure S1a, Supporting Information). When Au nanoparticles were not used in the synthesis, MPs with edge lengths of ~5 μm and thicknesses of several hundred nanometers were obtained.

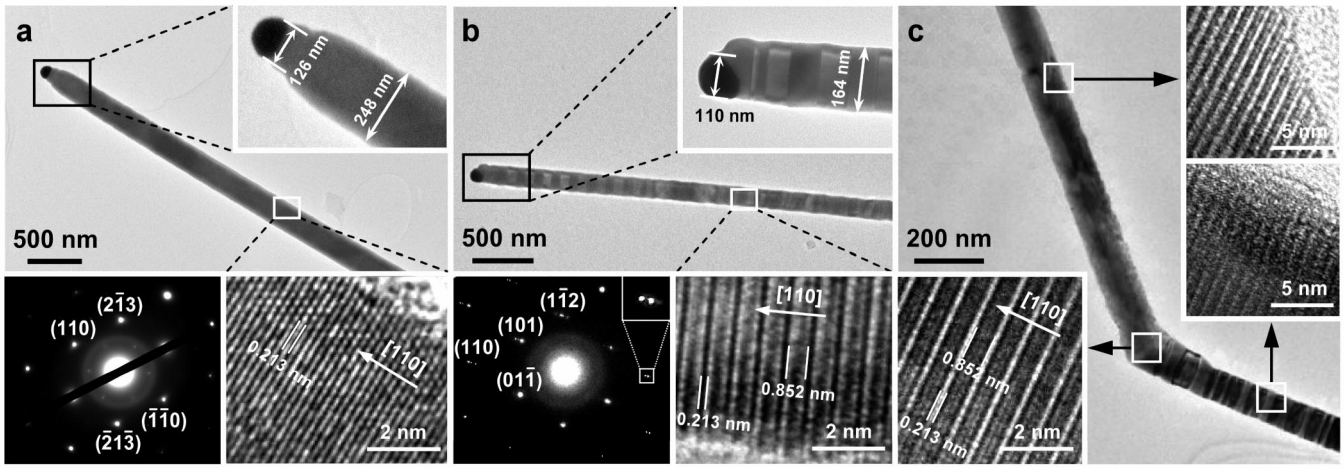

Figure 3. TEM images of a Sb_2Te_3 (a) T-NW, (b) T-NW with stacking faults, and (c) Z-NW with stacking faults. Insets of (a): bottom left, SAED pattern showing the growth of a rhombohedral crystal structure along the [110] direction; bottom right, HRTEM image showing the single-crystalline structure of a T-NW; top, high-magnification TEM image of the NW with a Sb_xTe_y/Au alloy particle. Insets of (b): bottom left, SAED pattern and bottom right, HRTEM image showing the twinned crystal structure and stacking faults found in some T-NWs; top, high-magnification TEM image of the NW with a Sb_xTe_y/Au alloy particle. Insets of (c): HRTEM images showing the twinned crystal structure and the stacking faults found in all Z-NWs.

EDX spectrometry confirms the 2:3 ratio of Sb and Te atoms in the t-NWs (Figure S2a, Supporting Information), and both XRD and TEM analyses show that the t-NWs exhibit the rhombohedral structure of bulk Sb_2Te_3 [space group: $R\bar{3}m$ (No. 166)] with lattice constants $a = 4.264$ and $c = 30.458$ Å (JCPDS file 71–0393) (Figures 2b and 2c). The TEM image and selected area electron diffraction (SAED) pattern obtained from the t-NW in Figure 2c confirm that the Sb_2Te_3 t-NW is single-crystalline and grows along the [110] direction. The high-resolution TEM (HRTEM) image taken from the area designated in Figure 2c also shows clear lattice fringes with 0.213-nm spacing, which corresponds to the (110) lattice planes of rhombohedral Sb_2Te_3 (Figure 2d).

Figures 3 and 4 show TEM images, SAED patterns, and HRTEM images obtained from a representative T-NW, Z-NW, NB, and NT. All SAED patterns are indexed to the same Sb_2Te_3 crystal structure as that of the t-NW, and the growth directions are also parallel to the [110] direction. Inspection of powder XRD (Figure S3, Supporting Information) patterns confirms the crystal structures of the Sb_2Te_3 T-NW/Z-NW mixture, NBs, and MPs. In contrast to the t-NWs, some (~20%) of the T-NWs and most of the Z-NWs show pairs of diffraction peaks along the different lattice directions, indicating the presence of twin domains (~20%) with alternating orientations along the [110] direction. The HRTEM images in the insets of Figure 3b,c clearly show these stacking faults found in some of the T-NWs and most of the Z-NWs.

Nanostructures with NT morphology were studied using cross-sectional EDX spectrometry, as shown in the STEM image in Figure 4c. These elemental line scans show that Sb and Te atoms are present throughout the nanostructure, but their concentrations decrease in the wire's center, reflecting its hollowness. The EDX mapping shown in the inset of Figure 4c confirms this tube structure.

In the TEM image in Figure 5a, the core/shell structure of the Sb_2Te_3/GeTe NW heterostructures can be seen from the uniform layer of GeTe (light) that coats the Sb_2Te_3 interior (dark). The diameter of the Sb_2Te_3 core is ~100 nm, and the thickness of the shell is ~50 nm. The SAED patterns in the insets of Figure 5a show two sets of diffraction patterns for Sb_2Te_3 and GeTe, confirming the single-crystalline nature of

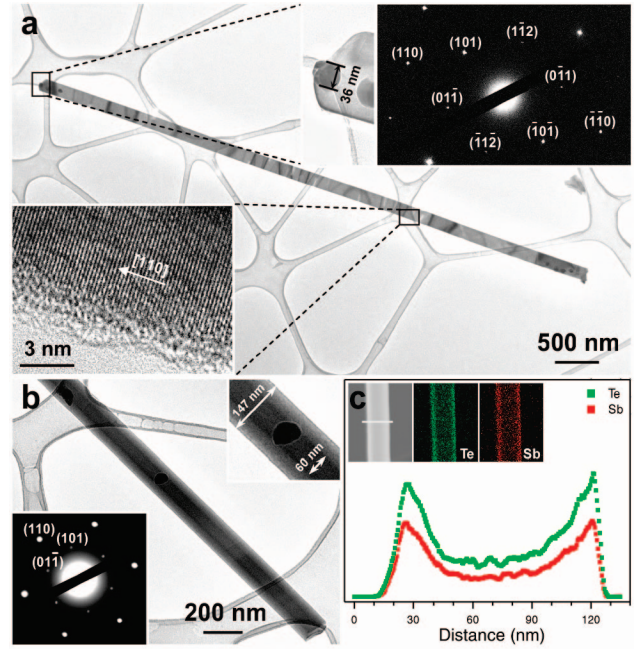

Figure 4. TEM images of a Sb_2Te_3 (a) NB and (b) NT. Insets of (a): top center, high-magnification TEM image of the NW's Sb_xTe_y/Au alloy particle; top right, SAED patterns showing growth along the [110] direction of a rhombohedral crystal; bottom, HRTEM image of the single-crystalline NB. Insets of (b): top, high-magnification TEM image of NT; bottom, SAED patterns indexed for rhombohedral Sb_2Te_3. (c) Cross-sectional EDX elemental line scans of a NT. Insets: bright-field STEM image of a NT with the corresponding EDX elemental mapping.

both core and shell. The growth direction of both regions is [110]. Crystal structures of each region of the Sb_2Te_3/GeTe core/shell NW heterostructures were also confirmed by powder XRD (Figure S4a, Supporting Information).

The HRTEM image in Figure 5b demonstrates that the interface between the Sb_2Te_3 core and the GeTe shell is sharp, with the lattice fringes continuous from core to shell. This observation indicates epitaxial growth of the GeTe layer on top of Sb_2Te_3. The lattice spacings of the core and the shell are 2.11 and 2.99 Å, respectively, corresponding to the (1–12) planes in Sb_2Te_3 and the (202) planes in GeTe. The EDX mapping in

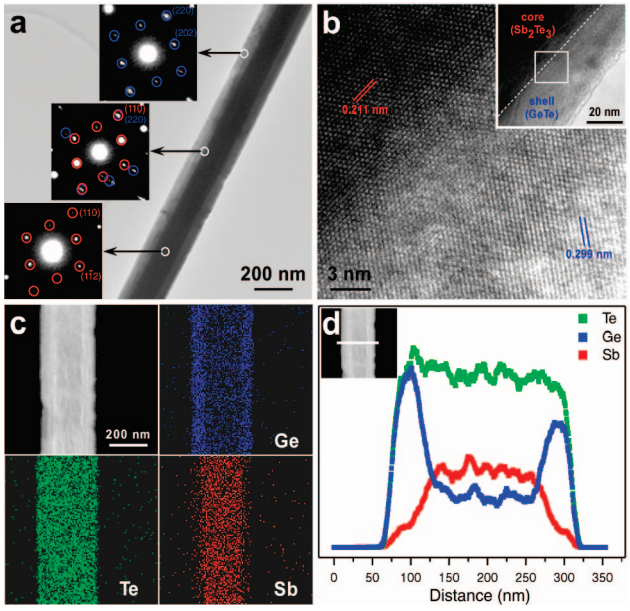

Figure 5. (a) TEM image of a core/shell NW showing the uniform GeTe shell coating the Sb_2Te_3 core. Insets: SAED patterns taken from the designated areas. Red (blue) circles indicate Sb_2Te_3 (GeTe) diffraction spots. (b) HRTEM image of a Sb_2Te_3/GeTe core/shell NW taken from the area designated in the inset; inset is a TEM image showing the core/shell interface. (c) Bright-field STEM image with the corresponding EDX elemental mapping and (d) cross-sectional EDX elemental line scans of a Sb_2Te_3/GeTe core/shell NB.

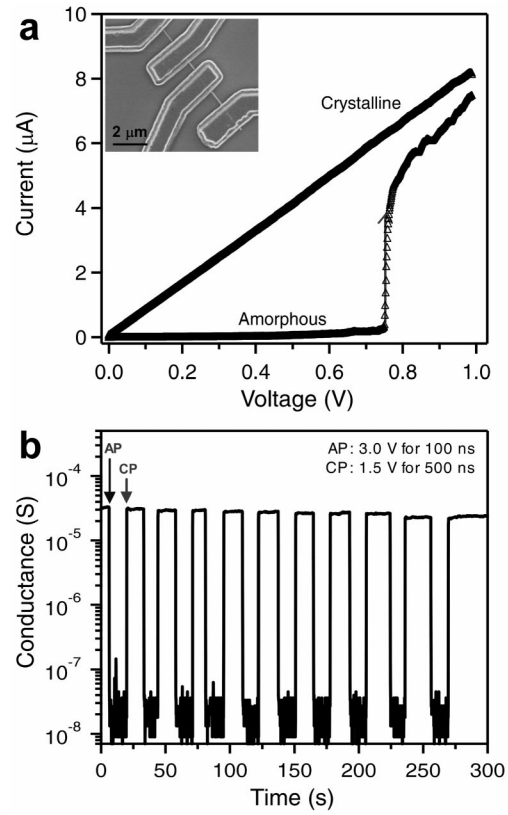

Figure 6. (a) $I-V$ characteristics of a Sb_2Te_3 NW device (99 nm diameter) with 100 kΩ load resistor after amorphization (AP: 2.9 V, 100 ns). Amorphous NWs spontaneously recrystallize when V exceeds the threshold voltage (here, 0.75 V). Inset: SEM image of a typical four-probe device. (b) Conductance of the same Sb_2Te_3 NW device through 10 pulsed switching cycles. The amorphization pulse (AP: 3.0 V, 100 ns) reduced the conductance below the preamplifer detection limit. The crystallization pulse (CP: 1.5 V, 500 ns) restored the device almost to its former conductance. $I-V$ measurements (not shown) indicated the ratio of resistances to be 10^3.

Figure 5c shows that the core/shell contrast observed in the bright-field STEM image arises from the spatial distribution of the Sb and Ge elements in the core and shell, respectively. The EDX elemental line scans in Figure 5d also show the localization of Sb and Ge, as well as the presence of Te throughout the whole structure (Figure S5, Supporting Information).

It should be noted that the synthesis of GeTe/Sb_2Te_3 core/shell NW heterostructures was also attempted by first preparing GeTe NWs and then depositing Sb_2Te_3. The product of this reaction, however, was a single-crystalline Sb_2Te_3 NW (Figures S6a,b middle panel, Supporting Information). EDX elemental mapping and line profiles of the NW confirm the absence of GeTe (Figure S6c,d, Supporting Information). In the top panel of Figure S6b, the XRD pattern of the control reaction, in which no Sb_2Te_3 precursor was introduced into the system but all other conditions were replicated, shows only a Au peak without GeTe peaks. This control indicates that raising the temperature to $T = 430$ °C, as is required for Sb_2Te_3 growth, causes the GeTe NWs to evaporate.

Current (I)−voltage (V) measurements were used to investigate the reversible, crystalline-to-amorphous phase transition of the Sb_2Te_3 NWs. These NWs were contacted with Cr/Au electrodes as described above. Figure 6a shows an $I-V$ curve obtained from a device containing a NW with a 99 nm diameter. The two-probe resistance of the as-fabricated nanowire device was 7.3 kΩ, but the recrystallized device resistance fell between 25 and 45 kΩ during repeated switching measurements. In comparison to the devices in their original single-crystalline state, recrystallized devices are always less conductive, most likely because the phase transition introduces defects into the wire. Amorphization of the 99 nm wire device, with a recrystallized resistance of 28.9 kΩ, by a 2.9 V pulse lasting 100 ns yielded an amorphous resistance of 28.0 MΩ. Four-probe measurements on similarly constructed devices confirmed that the increase in resistance results from the material's phase change rather than higher contact resistance. In a typical device, the resistance increases by a factor of 10^2-10^3. Upon linearly increasing a dc voltage, the current first rises steadily and then jumps suddenly at a device-dependent threshold voltage, marking the recrystallization event.

To explore the suitability of Sb_2Te_3 nanowires for phase-change memory applications, recrystallization was also induced with voltage pulses. Figure 6b displays the conductance plot of the 99 nm device during cycling of amorphization and recrystallization pulses. The optimized pulses for this cycling, shown in Figure 6b, are 3.0 V for 100 ns for amorphization and 1.5 V for 500 ns for recrystallization. The pulsed recrystallization voltage is higher than the device's dc threshold voltage shown in Figure 6a because Joule heating reduces the apparent threshold voltage in the dc measurement. Minor fluctuations in both the amorphous and crystalline device resistances during cycling reflect the changing material structure and defects inherent in phase-change processes. Several other devices each cycled 10−15 times using alternating pulses, but the maximum lifetime of the devices was not investigated. The conductance levels of the crystalline and amorphous states in these devices differed by 1−3 orders of magnitude.

Similar electrical measurements on the Sb_2Te_3/GeTe core/shell NW heterostructures show the ratio between the amorphous and crystalline device resistances to be 10^3-10^4 (Figure S7,

Supporting Information), an improvement over that of the Sb_2Te_3 nanowires. This increased ratio suggests that both materials undergo amorphization during the initial voltage pulse, and both likely return to their crystalline state. Because the two materials are arranged in an electrically parallel configuration, the least resistive path will transport the current; therefore, the large resistances measured for the amorphous state demonstrate that no less-resistive, crystalline path remains open for transport. Although it is possible that only the GeTe shell returns to the crystalline state and carries all the current through the wire, this situation is unlikely because the glass transition temperature of Sb_2Te_3 (77 °C[49]) is significantly lower than that of GeTe (145 °C[50]). If the wire reaches a temperature sufficient for the transition of GeTe, then the Sb_2Te_3 is predicted also to undergo a phase change.

Discussion

In vapor-transport syntheses previously reported in the literature, binary chalcogenide NWs have been prepared from a single precursor.[12,13,38,39] Although this method worked well for synthesizing GeTe NWs, the Sb_2Te_3 NWs prepared in this way were too short to study their phase-change properties. The modified vapor-transport method presented here controls the composition of the NWs by placing elemental precursors in different temperature regions of the furnace,[40] yielding long Sb_2Te_3 NWs with morphologies determined by the reaction conditions. Additionally, Sb_2Te_3/GeTe core/shell NW heterostructures have been synthesized by the *in situ* exchange of precursors. Figures 2−5 demonstrate that these synthetic methods allow control over the morphology of the Sb_2Te_3 nanostructures and of the Sb_2Te_3/GeTe core/shell heterostructures.

The high-magnification TEM images shown in the insets of Figures 2c and 3a,b suggest that Sb_2Te_3 NWs grow from the Au nanoparticles via the metal-catalyzed VLS mechanism.[51] TEM and EDX investigations confirm that the particles at the ends of the NWs have Sb_xTe_y/Au alloy composition, resulting from the influx of precursors into the Au nanoparticle during growth (Figure S2b, Supporting Information).

The presence of NBs suggests that, in addition to VLS growth, vapor−solid (VS) growth[26,31,34] also occurs under these reaction conditions. Upon increasing the flow rate from 80 to 140 sccm at the same reaction temperature (430 °C), NBs wider than the t-NWs appear, with no apparent change in the sizes of the Au alloy particles (Figures 2c and 4a). The additional lateral growth without change in catalyst size suggests that VS growth occurs preferentially at edges and widens the nanostructures. This preference can be explained by the layered structure[52] of Sb_2Te_3: the dangling bonds on the edges can incorporate atoms directly from the gas phase, while the surface of a layer is smooth and unreactive; consequently, the VS growth broadens the NWs into NBs.

The layered structure of Sb_2Te_3 can also explain the formation of NTs (∼5%) that are mixed in with the NBs (Figure 4b,c). When allowed sufficient time, layer-structured materials can form NTs by rolling up layers.[53–55] The SAED pattern of the NTs does not change when the electron beam scans along the length of the NTs, suggesting their origin as a single-crystalline sheet.

Temperature plays an important role in dictating the morphology of the Sb_2Te_3 nanostructures. Upon raising the growth temperature to 480 °C while maintaining the same flow rate of Ar gas (80 sccm), the Au alloy nanoparticles grow to 110–130 nm in diameter (3 times larger than the particle attached to the t-NW) (Figure 3a,b insets), which leads to thicker NWs (Figure S1b, Supporting Information). This additional swelling in the Au particle is most likely caused by the increased solubilities of the Sb and Te precursors in Au and their faster decomposition at elevated temperature. Also, some of the NWs (∼10%) grown at higher temperature exhibit a zigzag morphology (Figure S1b, Supporting Information) with stacking faults (∼20%) along the [110] growth direction (Figure 3c inset). About 20% of the T-NWs also exhibit these same stacking faults (Figure 3b inset). At higher temperature and the resulting faster growth rate, the reaction's kinetics might favor stacking faults over single crystallinity.[56]

For the synthesis of Sb_2Te_3/GeTe core/shell heterostructures, the reaction mechanism can be understood as follows: the core Sb_2Te_3 NWs or NBs first form by VLS and VS mechanisms; then, the core nanostructures serve as nuclei, and the GeTe shells grow on the cores through a VS mechanism.[20,28,30,32,33,36,37] Interestingly, XRD analysis suggests that the shell composition depends upon the time interval between the Sb_2Te_3 and GeTe growth (Figure S4, Supporting Information). For example, when the time interval was shorter than 5 min, a shell composed of $Ge_{0.95}Sb_2Te_4$ (rhombohedral, JCPDS 89-1064) was formed, whereas when it was between 5 and 40 min, a dual shell ($Ge_{0.95}Sb_2Te_4$ inner shell and GeTe outer shell) was formed. These findings indicate that a reaction between the residual Sb_2Te_3 precursor and the evaporated GeTe precursor is responsible for the formation of a $Ge_{0.95}Sb_2Te_4$ shell. In the presented reaction scheme, core/shell heterostructures form when only Sb_2Te_3 NWs, but not GeTe NWs, are used as cores. This result can be attributed to the instability of the GeTe NWs at the conditions necessary for growing Sb_2Te_3 shells.

$I-V$ characteristics of Sb_2Te_3 NWs are similar to those of NWs of other chalcogenides, including GeTe[12,13] and $Ge_2Sb_2Te_5$[14,40] (Figure 6a). The increase in resistance by a factor of 10^2-10^3 for Sb_2Te_3 NWs falls between the values reported for NWs of GeTe[12,13] and $Ge_2Sb_2Te_5$,[14,40] 10^3-10^7 and 10^2, respectively. Similarly, the observed voltages for recrystallization, typically ranging from 0.6 to 2.0 V, are comparable to those measured for devices constructed from other chalcogenide NWs.

$I-V$ characteristics of the Sb_2Te_3/GeTe core/shell NW heterostructures demonstrate improved properties for phase-change memory switching as compared to those of the Sb_2Te_3 NWs. Devices are less likely to be damaged by currents ∼100 μA and survive phase transitions without the inclusion of a current-limiting resistor. This robustness is common to phase-change materials containing Ge and could result either from

(49) Das, V. D.; Soundararajan, N.; Pattabi, M. *J. Mater. Sci.* **1987**, *22*, 3522–3528.
(50) Bahl, S. K.; Chopra, K. L. *J. Appl. Phys.* **1970**, *41*, 2196–2212.
(51) Wagner, R. S.; Ellis, W. C. *Appl. Phys. Lett.* **1964**, *4*, 89–90.
(52) Venkatasubramanian, R.; Siivola, E.; Colpitts, T.; O'Quinn, B. *Nature* **2001**, *413*, 597–602.
(53) Chopra, N. G.; Luyken, R. J.; Cherrey, K.; Crespi, V. H.; Cohen, M. L.; Louie, S. G.; Zettl, A. *Science* **1995**, *269*, 966–967.
(54) Gautam, U. K.; Vivekchand, S. R. C.; Govindaraj, A.; Kulkarni, G. U.; Selvi, N. R.; Rao, C. N. R. *J. Am. Chem. Soc.* **2005**, *127*, 3658–3659.
(55) Hu, P. A.; Liu, Y. Q.; Fu, L.; Cao, L. C.; Zhu, D. B. *Appl. Phys. A: Mater. Sci. Process.* **2005**, *80*, 1413–1417.
(56) Hao, Y.; Meng, G.; Wang, Z. L.; Ye, C.; Zhang, L. *Nano Lett.* **2006**, *6*, 1650–1655.

the support of the GeTe shell itself or from alloying to form a Ge−Sb−Te compound.

Conclusions

By choosing the reaction conditions and the location of precursors carefully, nanostructures of Sb_2Te_3 and Sb_2Te_3/GeTe core/shell NW heterostructures have been synthesized. This approach controls the morphology of the nanostructures and offers a simple method for synthesizing nanostructures with built-in heterojunctions. The Sb_2Te_3 NWs reported here can be useful for further study of this phase-change material and its potential applications in electronic memory devices. Similarly, the Sb_2Te_3/GeTe NW heterostructures should be useful for fundamental studies of phase-change materials, such as strain- and interface-induced alteration of their phase-change behaviors and material diffusion/doping at the nanoscale.

Acknowledgment. This work was supported by Samsung Electronics Co., the National Science Foundation, the Packard Foundation, and the Korean Research Foundation (KRF-2006-352-C00040). We are grateful to Chun Liang Yu, Hongtao Wang, David Bell, and David Lange for assistance with characterization of the nanostructures, to Abram Falk, Yuan Lu, and Steve Shepard for assistance with fabrication of the electrical devices, and to Nathalie de Leon for helpful discussions. We also acknowledge the Harvard Nanoscale Science and Engineering Center REU program, the Harvard Program for Research in Science and Engineering, and the Harvard College Research Program for supporting this research.

Supporting Information Available: Figure S1, histograms of the diameters of t-NWs and a T-NW/Z-NW mixture, and of the widths of NBs and SEM images of the mixture of T-NWs and Z-NWs, NBs, and MPs; Figure S2, energy-dispersive X-ray spectra of a t-NW and Au-alloy nanoparticle; Figure S3, powder XRD of Sb_2Te_3 nanostructures; Figure S4, powder XRD of Sb_2Te_3/GeTe core/shell NW heterostructures; Figure S5, EDX elemental line scans of NW heterostructures; Figure S6, TEM image, SAED pattern, powder XRD, EDX elemental mapping, and cross-sectional EDX elemental line scans of GeTe/Sb_2Te_3 core/shell NW heterostructures; Figure S7, $I-V$ curve of a Sb_2Te_3/GeTe core/shell NW heterostructure. This material is available free of charge via the Internet at http://pubs.acs.org.

JA711481B